Polyhedron 90 (2015) 58–68

Contents lists available at ScienceDirect

Polyhedron

journal homepage: www.elsevier.com/locate/poly

Four coordination compounds constructed from 1,10-phenanthroline and semi-flexible and flexible carboxylic acids: Hydrothermal synthesis, optical properties and photocatalytic performance

Chong-Chen Wang [a,b,*], Yan-Qiu Zhang [a], Tian Zhu [a], Xiao-Ying Zhang [c], Peng Wang [a], Shi-Jie Gao [a]

[a] Key Laboratory of Urban Stormwater System and Water Environment (Ministry of Education), Beijing University of Civil Engineering and Architecture, Beijing 100044, China
[b] Beijing Engineering Research Center of Sustainable Urban Sewage System Construction and Risk Control, Beijing University of Civil Engineering and Architecture, Beijing 100044, China
[c] Shandong Electric Power Engineering consulting institute Co., Ltd., Jinan 250100, China

ARTICLE INFO

Article history:
Received 6 December 2014
Accepted 28 January 2015
Available online 12 February 2015

Keywords:
Coordination compounds
Optical energy gap
Photocatalysis
Degradation
Organic dye

ABSTRACT

Four novel coordination compounds based on d^{10} metals, 1,10-phenanthroline (phen) and 2,2′,3,3′-oxydiphthalic acid (2,2′,3,3′-odpt), 3,5-di(3,4-dicarboxylphenyloxy)benzoic acid (dcpb) or 1,3-(3′,4′-carboxylphenoxy)benzene (cpb), namely $[Co_2(phen)_4(2,2',3,3'\text{-}H_2odpt)_2]\cdot 14H_2O$ (**1**), $[Co_2(phen)_4(H_4dcpb)_2]\cdot 14H_2O$ (**2**), $[Cu(phen)(H_3dcpb)]$ (**3**) and $[Mn(phen)_2(H_2cpb)]$ (**4**), have been synthesized under hydrothermal conditions and characterized by the methods of single crystal X-ray diffraction, FTIR, elemental analysis and UV–Vis diffuse spectroscopy. The isostructural compounds **1** and **2** consist of discrete neutral $[Co_2(phen)_4(L)_2]$ (L = 2,2′,3,3′-odpt for **1** and dcpb for **2**) units and lattice water molecules, forming 3D frameworks with the aid of rich hydrogen bonding interactions. Compounds **3** is built up of discrete neutral $[Cu(phen)(H_3dcpb)]$ units to construct a 3D framework via π–π stacking interactions. Compound **4** consists of 1D neutral $[Mn(phen)_2(H_2cpb)]$ helix chains, further forming a 3D framework via rich hydrogen bonding interactions. The photocatalytic activities of degradation of methylene blue (MB) and methyl orange (MO) in compounds **1**–**4** under UV light irradiation were determined, and the results revealed that compound **4** can decompose MB and MO efficiently. The different degradation efficiencies of compounds **1**–**4** implied that the HOMO–LUMO gap should be utilized to describe the discrete character of the light-induced transitions in the coordination compounds.

1. Introduction

Coordination compounds which exhibit a high surface area and large pore volume are of great current interest for their specific structural features [1–7] and potential applications, such as gas storage [8–10], separation [11,12], carbon dioxide capture [13] and catalysis [14]. Just recently, an increasing number of reports on coordination compounds as photocatalysts have appeared to indicate that they provide a unique opportunity for integrating different molecular functional blocks to obtain good performance of organic pollutant degradation [15–21], CO_2 reduction [22–24] and Cr(VI) reduction [25,26]. Compared to traditional semiconductor photocatalytic systems, photoactive coordination compounds have some advantages to act as efficient photocatalysts: (i) the well-defined crystalline structures of coordination compounds are beneficial in the characterization and study of the structure–property relationship of these solid photocatalysts; (ii) the modular nature of the synthesis of coordination compounds allows the rational design and fine tuning of these catalysts at the molecular level, allowing the electronic structure of the coordination compounds catalysts to be easily tailored; (iii) the structural features of tunable active sites (*i.e.*, metal-oxo clusters and organic linkers) in coordination compounds lead to more efficiency in solar harnessing; (iv) the intrinsic porosity and high surface area can facilitate fast transport guest molecules through the open channels, which is very essential for a high photocatalytic reaction efficiency.

As is well known, the construction of coordination compounds is mainly dependent on the combination of several factors, such as the organic ligands, solvents, metal atoms and counter-ions [1–3,5,17,18,27]. Polycarboxylate ligands, as good candidates for the construction of coordination compounds, have aroused a good deal of interest from chemists. 2,2′,3,3′-Oxydiphthalic acid (2,2′,3,3′-odpt) had been used as a flexible and semi-flexible

* Corresponding author. Tel./fax: +86 10 6832 2124.
E-mail address: chongchenwang@126.com (C.-C. Wang).

http://dx.doi.org/10.1016/j.poly.2015.01.042
0277-5387/

exo-multidentate ligand for the design and construction of novel coordination compounds due to its versatile coordination modes [28,29]. In this paper, in addition to 2,2′,3,3′-odpt, two special exo-multidentate ligands, 3,5-di(3,4-dicarboxylphenyloxy) benzoic acid (dcpb) and 1,3-(3′,4′-carboxylphenoxy) benzene (cpb) were introduced to construct four transition metal-based compounds, namely $[Co_2(phen)_4(2,2',3,3'\text{-}H_2odpt)_2]\cdot 14H_2O$ (**1**), $[Co_2(phen)_4(H_4dcpb)_2]\cdot 14H_2O$ (**2**), $[Cu(phen)(H_3dcpb)]$ (**3**) and $[Mn(phen)_2(H_2cpb)]$ (**4**), with the aid of 1,10-phenanthroline (phen). The optical gaps, photocatalytic activities and possible degradation mechanism towards methylene blue (MB) and methyl orange (MO) in aqueous solution were studied.

2. Experimental

2.1. Materials and methods

All chemicals were commercially available reagent grade and used without further purification. Elemental analyses were obtained using an Elementar Vario EL-III instrument. FTIR spectra, in the region 400–4000 cm^{-1}, were recorded on a Nicolet 6700 Fourier Transform infrared spectrophotometer. UV–Vis diffuse reflectance spectra of solid samples were measured from 200 to 1200 nm with a Perkin Elmer Lamda 650S spectrophotometer, in which barium sulfate ($BaSO_4$) was used as the standard with 100% reflectance. Powder X-ray diffraction (PXRD) patterns were recorded using a Dandonghaoyuan DX-2700B diffractometer employing Cu Kα radiation. The morphology of the compounds was studied with a Hitachi SU8020 scanning electron microscope (SEM).

2.2. Synthesis of the coordination compounds

2.2.1. Synthesis of $[Co_2(phen)_4(2,2',3,3'\text{-}H_2odpt)_2]\cdot 14H_2O$ (1)

A mixture of $CoCl_2\cdot 6H_2O$ (0.3 mmol, 0.0714 g), 2,2′,3,3′-oxydiphthalic acid (0.3 mmol, 0.1038 g) and 1,10-phen (0.6 mmol, 0.1189 g) with a molar ratio of 1:1:2 was sealed in a 25 mL Teflon-lined stainless steel Parr bomb containing deionized H_2O (20 mL), heated at 160 °C for 72 h, and then cooled down to room temperature. Orange block-like crystals were isolated and washed with deionized water and ethanol (yield 72% based on $CoCl_2\cdot 6H_2O$). *Anal.* Calc. for **1**, $C_{80}H_{61}Co_2N_8O_{25}$: C, 58.1; N, 6.8; H, 3.7. Found: C, 58.2; N, 6.7; H, 3.8%. IR (KBr) cm^{-1}: 3446.94, 3074.34, 1712.15, 1591.26, 1518.09, 1451.89, 1427.10, 1390.62, 1247.46, 1144.79, 1104.06, 988.27, 867.82, 848.06, 776.16, 726.80, 690.05, 642.66, 601.03, 511.68, 423.21.

2.2.2. Synthesis of $[Co_2(phen)_4(H_4dcpb)_2]\cdot 7H_2O$ (2)

Light pink block-like crystals of **2** (yield 87% based on $CoCl_2\cdot 6H_2O$) were synthesized from a mixture of $CoCl_2\cdot 6H_2O$ (0.3 mmol, 0.0714 g), 3,5-di(3,4-dicarboxylphenyloxy)benzoic acid (0.3 mmol, 0.1446 g) and 1,10-phen (0.6 mmol, 0.1189 g) with a molar ratio of 1:1:2 under the same conditions as for **1**. *Anal.* Calc. for **2**, $C_{94}H_{68}Co_2N_8O_{30}$: C, 59.1; N, 5.9; H, 3.6. Found: C, 59.0; N, 5.8; H, 3.7% IR(KBr) cm^{-1}: 3311.56, 3035.44, 2002.12, 1689.71, 1427.13, 1361.51, 1252.81, 1215.41, 1123.74, 1103.76, 1008.12, 908.36, 882.87, 866.55, 849.70, 829.42, 805.74, 774.76, 726.76, 673.28, 640.57, 591.96, 530.44, 511.60, 481.78, 422.21.

2.2.3. Synthesis of $[Cu(phen)(H_3dcpb)]$(3)

Blue block-like crystals of **3** (yield 72% based on $CuCl_2\cdot 2H_2O$) were synthesized from a mixture of $CuCl_2\cdot 2H_2O$ (0.3 mmol, 0.0511 g), 3,5-di(3,4-dicarboxylphenyloxy)benzoic acid (0.3 mmol, 0.1446 g) and 1,10-phen (0.6 mmol, 0.1189 g) with a molar ratio of 1:1:2 under the same conditions as for **1**. *Anal.* Calc. for **3**, $C_{35}H_{20}CuN_2O_{12}$: C, 59.0; N, 1.9; H, 2.8. Found: C, 59.1; N, 1.9; H, 2.9%. IR(KBr) cm^{-1}: 3566.74, 3070.37, 2920.67, 2594.15, 1710.42, 1577.81, 1518.03, 1494.20, 1367.55, 1300.31, 1251.73, 1221.12, 1137.87, 1066.45, 1005.79, 967.18, 851.73, 803.43, 776.48, 725.27, 700.64.

2.2.4. Synthesis of $[Mn(phen)_2(H_2cpb)]$(4)

Pink block-like crystals of **4** (yield 86% based on $MnCl_2\cdot 4H_2O$) were synthesized from a mixture of $MnCl_2\cdot 4H_2O$ (0.3 mmol, 0.0594 g), 1,3-(3′,4′-carboxylphenoxy)benzene (0.3 mmol, 0.1314 g) and 1,10-phen (0.6 mmol, 0.1189 g) with a molar ratio of 1:1:2 under the same conditions as for **1**. *Anal.* Calc. for **4**, $C_{46}H_{28}MnN_4O_{10}$: C, 64.8; N, 6.6; H, 3.3. Found: C, 65.0; N, 6.5; H, 3.5%. IR(KBr) cm^{-1}: 1688.06, 1590.68, 1557.50, 1517.73, 1478.62, 1423.15, 1363.86, 1261.76, 1217.43, 1123.69, 984.42, 911.63, 847.06, 771.68, 729.65, 638.08, 506.41, 443.08.

Table 1
Details of X-ray data collection and refinement for compounds **1**–**4**.

	1	2	3	4
Formula	$C_{80}H_{61}Co_2N_8O_{25}$	$C_{94}H_{68}Co_2N_8O_{30}$	$C_{35}H_{20}CuN_2O_{12}$	$C_{46}H_{28}MnN_4O_{10}$
M	1652.23	1907.42	724.07	851.66
Crystal system	triclinic	triclinic	triclinic	triclinic
Space group	$P\bar{1}$	$P\bar{1}$	$P\bar{1}$	$P\bar{1}$
a (Å)	13.9110(11)	11.0290(9)	10.1010(8)	11.1140(9)
b (Å)	13.9221(12)	13.8509(11)	10.2930(8)	12.8430(11)
c (Å)	22.2332(19)	14.7551(12)	16.4670(13)	14.1460(12)
α (°)	88.592	87.337(2)	90.6530(10)	85.183(2)
β (°)	75.8540	86.822(2)	103.628(2)	75.5180(10)
γ (°)	63.8540	71.0420(10)	116.279(3)	75.4110(10)
V ($Å^3$)	3731.0(5)	2127.5(3)	1478.7(2)	1891.5(3)
Z	2	1	2	2
μ (Mo Kα) (mm^{-1})	0.533	0.483	0.815	0.420
Total reflections	19149	10745	7541	9658
Unique	12977	7369	5115	6550
F(000)	1702	982	738	874
Goodness-of-fit (GOF) on F^2	0.964	1.103	1.057	1.019
R_{int}	0.0557	0.0187	0.0233	0.0329
R_1	0.0655	0.0782	0.0392	0.0508
wR_2	0.0953	0.2260	0.0839	0.0651
R_1 (all data)	0.1643	0.1122	0.0555	0.1009
wR_2 (all data)	0.1072	0.2552	0.0887	0.0723
Largest differences in peak and hole (e/$Å^3$)	0.535, −0.350	1.238, −0.640	0.432, −0.439	0.326, −0.306

2.3. X-ray crystallography

X-ray single-crystal data collection for compounds **1**–**4** was performed with a Bruker CCD area detector diffractometer with graphite-monochromatized Mo Kα radiation (λ = 0.71073 Å) using the $\varphi - \omega$ mode at 298(2) K. The SMART software [30] was used for data collection and the SAINT software [31] for data extraction. Empirical absorption corrections were performed with the SADABS program [32]. The structures were solved by direct methods (SHELXS-97) [33] and refined by the full-matrix-least squares technique on F^2 with anisotropic thermal parameters for all of the non-hydrogen atoms (SHELXL-97) [33]. All hydrogen atoms were located by Fourier difference synthesis and geometrical analysis. These hydrogen atoms were allowed to ride on their respective parent atoms. All structural calculations were carried out using the SHELX-97 program package [33]. Crystallographic data and structural

Table 2
Selected bond lengths (Å) and angles (°) for compounds **1**–**4**.

(**1**)					
Bond lengths (Å)					
Co(1)–O(4)#1	2.054(3)	Co(1)–O(3)	2.099(3)	Co(1)–N(2)	2.104(4)
Co(1)–N(3)	2.110(4)	Co(1)–N(4)	2.136(5)	Co(1)–N(1)	2.148(4)
Co(2)–O(12)#2	2.048(4)	Co(2)–O(13)	2.105(4)	Co(2)–N(6)	2.142(5)
Co(2)–N(8)	2.146(6)	Co(2)–N(7)	2.147(5)	Co(2)–N(5)	2.185(5)
Bond angles (°)					
O(4)#1–Co(1)–O(3)	95.46(13)	O(4)#1–Co(1)–N(2)	96.86(14)		
O(3)–Co(1)–N(2)	95.28(16)	O(4)#1–Co(1)–N(3)	90.59(16)		
O(3)–Co(1)–N(3)	91.10(14)	N(2)–Co(1)–N(3)	169.67(19)		
O(4)#1–Co(1)–N(4)	168.64(19)	O(3)–Co(1)–N(4)	86.10(15)		
N(2)–Co(1)–N(4)	94.2(2)	N(3)–Co(1)–N(4)	78.1(2)		
O(4)#1–Co(1)–N(1)	92.09(13)	O(3)–Co(1)–N(1)	170.77(15)		
N(2)–Co(1)–N(1)	78.50(18)	N(3)–Co(1)–N(1)	94.14(17)		
N(4)–Co(1)–N(1)	87.54(17)	O(12)#2–Co(2)–O(13)	92.64(15)		
O(12)#2–Co(2)–N(6)	96.09(17)	O(13)–Co(2)–N(6)	95.38(19)		
O(12)#2–Co(2)–N(8)	165.6(2)	O(13)–Co(2)–N(8)	87.50(18)		
N(6)–Co(2)–N(8)	98.2(2)	O(12)#2–Co(2)–N(7)	88.3(2)		
O(13)–Co(2)–N(7)	96.93(16)	N(6)–Co(2)–N(7)	166.7(2)		
N(8)–Co(2)–N(7)	77.4(2)	O(12)#2–Co(2)–N(5)	94.54(17)		
O(13)–Co(2)–N(5)	169.69(18)	N(6)–Co(2)–N(5)	76.5(2)		
N(8)–Co(2)–N(5)	87.38(19)	N(7)–Co(2)–N(5)	90.7(2)		
Symmetry transformations used to generate equivalent atoms: #1 $-x+1, -y+1, -z+1$; #2 $-x+1, -y+2, -z$.					
(**2**)					
Bond lengths (Å)					
Co(1)–O(5)	2.068(3)	Co(1)–O(6)#1	2.069(3)	Co(1)–N(4)	2.118(4)
Co(1)–N(3)	2.123(4)	Co(1)–N(2)	2.138(4)	Co(1)–N(1)	2.158(4)
Bond angles (°)					
O(5)–Co(1)–O(6)#1	92.42(12)	O(5)–Co(1)–N(4)	97.20(14)		
O(6)#1–Co(1)–N(4)	94.42(14)	O(5)–Co(1)–N(3)	93.17(14)		
O(6)#1–Co(1)–N(3)	171.70(15)	N(4)–Co(1)–N(3)	78.80(16)		
O(5)–Co(1)–N(2)	88.71(14)	O(6)#1–Co(1)–N(2)	86.69(14)		
N(4)–Co(1)–N(2)	173.93(16)	N(3)–Co(1)–N(2)	99.56(17)		
O(5)–Co(1)–N(1)	165.89(14)	O(6)#1–Co(1)–N(1)	86.55(13)		
N(4)–Co(1)–N(1)	96.91(15)	N(3)–Co(1)–N(1)	89.50(15)		
N(2)–Co(1)–N(1)	77.19(15)				
Symmetry transformations used to generate equivalent atoms: #1 $-x+1, -y+1, -z+1$.					
(**3**)					
Bond lengths (Å)					
Cu(1)–O(5)	1.9237(18)	Cu(1)–O(10)	1.9758(18)	Cu(1)–N(1)	1.988(2)
Cu(1)–N(2)	1.995(2)				
Bond angles (°)					
O(5)–Cu(1)–O(10)	91.81(8)	O(5)–Cu(1)–N(1)	170.19(8)		
O(10)–Cu(1)–N(1)	94.03(8)	O(5)–Cu(1)–N(2)	93.00(8)		
O(10)–Cu(1)–N(2)	166.56(8)	N(1)–Cu(1)–N(2)	83.07(9)		
(**4**)					
Bond lengths (Å)					
Mn(1)–O(6)#1	2.134(2)	Mn(1)–O(1)	2.1489(19)	Mn(1)–N(4)	2.275(2)
Mn(1)–N(2)	2.284(3)	Mn(1)–N(1)	2.315(3)	Mn(1)–N(3)	2.325(2)
Bond angles (°)					
O(6)#1–Mn(1)–O(1)	97.40(8)	O(6)#1–Mn(1)–N(4)	108.67(9)		
O(1)–Mn(1)–N(4)	87.66(9)	O(6)#1–Mn(1)–N(2)	87.98(10)		
O(1)–Mn(1)–N(2)	106.41(8)	N(4)–Mn(1)–N(2)	156.92(10)		
O(6)#1–Mn(1)–N(1)	158.96(10)	O(1)–Mn(1)–N(1)	94.85(8)		
N(4)–Mn(1)–N(1)	88.83(10)	N(2)–Mn(1)–N(1)	72.14(11)		
O(6)#1–Mn(1)–N(3)	87.20(8)	O(1)–Mn(1)–N(3)	159.40(9)		
N(4)–Mn(1)–N(3)	71.88(10)	N(2)–Mn(1)–N(3)	93.78(10)		
N(1)–Mn(1)–N(3)	87.32(9)				
Symmetry transformations used to generate equivalent atoms: #1 $x, y+1, z$; #2 $x, y-1, z$.					

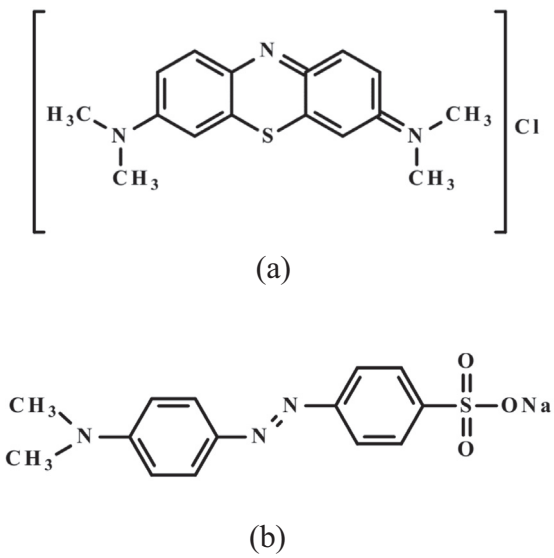

Scheme 1. The structure of (a) methylene blue (MB) and (b) methyl orange (MO).

refinements for compounds **1**–**4** are summarized in Table 1. Selected bond lengths and angles for all compounds are listed in Table 2.

2.4. Photocatalytic degradation of MB and MO

Methylene blue (MB) with the molecular formula $C_{16}H_{18}N_3SCl$ (FW 319.85 g/mol) and methyl orange (MO) with the molecular formula $C_{14}H_{14}N_3NaO_3S$ (FW 327.33 g/mol), as illustrated in Scheme 1, are difficult to degrade in wastewater and were used as model organic dye pollutants to evaluate the photocatalytic activities of compounds **1**–**4** at room temperature and under 500 W Hg lamp irradiation in a photocatalytic assessment system (Beijing Aulight Co. Ltd.). The distance between the light source and the beaker containing the reaction mixture was fixed at 5 cm. 50 mg of powder for each compound, with a particle size less than 147 μm and obtained by grinding the as-prepared single crystals, were put into 200 ml of MB (10 mg/L) or MO (30 mg/L) aqueous solution in a 300 ml flask. Prior to irradiation, the suspension was magnetically stirred in the dark for 120 min to ensure the establishment of an adsorption/desorption equilibrium. During the photodegradation reaction, stirring was maintained to keep the mixture in suspension. One milliliter sample was extracted at regular intervals using a 0.45 μm syringe filter (Shanghai Troody) for analysis. A Laspec Alpha-1860 spectrometer was used to monitor the changes of the dye absorbance in the range 400–800 nm in a 1 cm path length spectrometric quartz cell. The MB and MO concentrations were estimated by the absorbance at 664 and 463 nm, respectively.

3. Results and discussion

3.1. Structural description

3.1.1. Compounds *1* and *2*

Both compounds **1** and **2** crystallize in the triclinic space group P-1 and possess similar crystal structures, except for the organic carboxylic acid (2,2′,3,3′-H_4odpt in **1** and H_5dcpb in **2**) and the number of the lattice water molecules (14 lattice water molecules and 6 lattice water molecules respectively). Hence, only the structure of **1** is described in detail. The crystal structure analysis reveals that the compound **1** consists of the discrete neutral $[Co_2(phen)_4(2,2',3,3'\text{-}H_2odpt)_2]$ complex and fourteen lattice water molecules. The Co(II) ion, in an octahedral geometry, is six-coordinated by four nitrogen atoms from two different phen ligands and two oxygen atoms from two different 2,2′,3,3′-H_2odpt^{2-} ligands, in which one nitrogen and oxygen atom (N1 and O3) occupy the axial positions, and the remaining three nitrogen atoms (N2, N3 and N4) and one oxygen atom ($O4^{\#1}$) lie in the four sites of the equatorial plane, as shown in Fig. 1(a). The Co–O and Co–N bond distances compare with the normal values for these bonds [7,34]. In the equatorial plane, the $O4^{\#1}$–Co1–N2, $O4^{\#1}$–Co1–N3, N2–Co1–N4 and N3–Co1–N4 bond angles are 96.86(14), 91.10(14), 94.2(2) and 78.1(2)°, respectively, and the N1–Co1–O3 bond angle is 170.77(15)°, implying the Co-centered coordination octahedron is slightly distorted. The partly deprotonated 2,2′,3,3′-H_2odpt^{2-} ligands act as both bis-monodentate ligands to link two Co(II) ions and counter-ions to compensate the charge of $[Co(phen)_2]^{2+}$, which is very different from the coordination modes reported previously [28,29]. The dihedral angles between the phenyl rings of the 2,2′,3,3′-H_2odpt^{2-} ligands are 88.3(2)°, exhibiting the typical V-shaped mode with the presence of an O atom. The neighboring $[Co_2(phen)_4(2,2',3,3'\text{-}H_2odpt)_2]$ units are further linked into a 3D framework by rich hydrogen bonding interactions, as illustrated in Fig. 1(b) and (c) and Table 3.

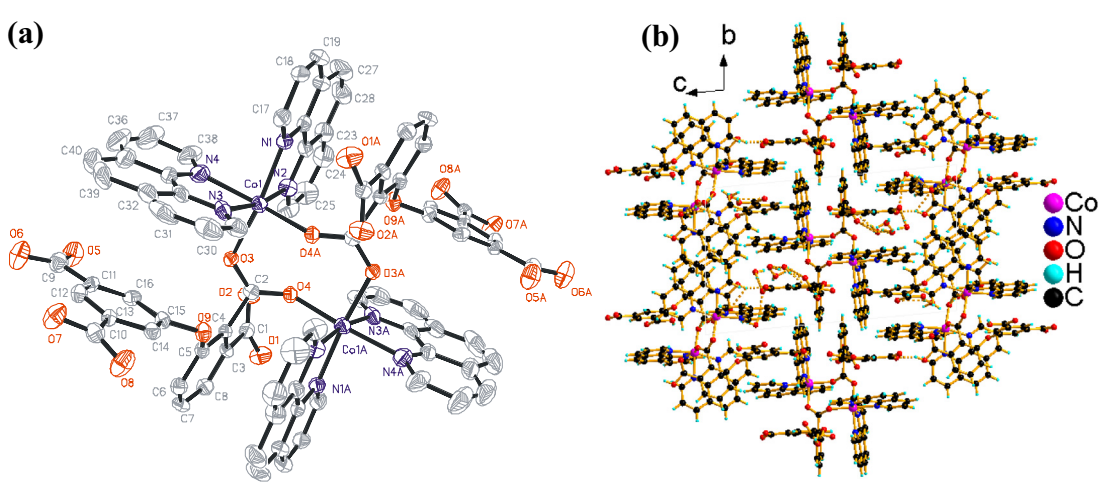

Fig. 1. (a) Asymmetric unit of $[Co_2(phen)_4(2,2',3,3'\text{-}H_2odpt)_2]\cdot 14H_2O$ (**1**) and coordination environments around the Co(II) atoms. (b) Packing view of the 3D framework built from $[Co_2(phen)_4(2,2',3,3'\text{-}H_2odpt)_2]$ and lattice water molecules via rich hydrogen bonding interactions along the *a*-axis for compound **1**.

Table 3
Hydrogen bonds for compounds **1**–**4**.

D–H	d(D–H)	d(H–A)	<DHA	d(D–A)	A
(**1**)					
O1–H1	0.82	1.73	170.14	2.542	O7 [$x-1, y, z$]
O10–H10	0.82	1.687	156.19	2.46	O5 [$-x+1, -y+2, -z$]
O14–H14	0.82	1.838	159.29	2.621	O22 [$x-1, y+1, z$]
O19–H19C	0.85	2.181	179.04	3.031	O3
O19–H19D	0.85	2.165	179.41	3.015	O5
O20–H20C	0.85	2.419	151.23	3.191	O2
O20–H20C	0.85	2.463	124.18	3.024	O24
O20–H20D	0.85	2.069	150.46	2.84	O7 [$x-1, y, z$]
O21–H21C	0.85	2.294	152.38	3.072	O11 [$x, y-1, z+1$]
O21–H21D	0.85	2.293	150.46	3.062	O13 [$x, y-1, z+1$]
O22–H22C	0.85	1.956	169.68	2.797	O21 [$-x+1, -y, -z+1$]
O22–H22D	0.85	2.097	170.56	2.939	O25 [$-x+1, -y, -z+1$]
O23–H23C	0.85	1.992	178.54	2.842	O6 [$x-1, y, z$]
O23–H23D	0.85	2.051	179.09	2.901	O20
O24–H24C	0.85	2.353	160.15	3.166	O2
O24–H24C	0.85	2.528	118.22	3.024	O20
O24–H24D	0.85	1.924	160.35	2.74	O19
O25–H25C	0.85	2.188	157.55	2.991	O6 [$-x+1, -y+1, -z+1$]
O25–H25D	0.85	2.162	159.98	2.975	O11 [$x, y-1, z+1$]
(**2**)					
O1–H1	0.82	1.883	160.65	2.671	O8 [$x-1, y, z$]
O4–H4	0.82	1.636	158.81	2.419	O15
O10–H10	0.82	1.647	176.69	2.466	O9
O13–H13C	0.85	2.145	171.66	2.988	O3
O13–H13D	0.85	2.049	170.84	2.891	O8 [$x-1, y-1, z$]
O14–H14C	0.85	2.123	174.87	2.97	O6
O14–H14D	0.85	2.259	174.64	3.106	O11 [$-x+1, -y+2, -z+2$]
O15–H15C	0.85	2.14	168.75	2.978	O2 [$x, y-1, z$]
O15–H15D	0.85	1.985	167.86	2.821	O9 [$x-1, y-1, z$]
O15–H15D	0.85	2.482	114.59	2.939	O8 [$x-1, y-1, z$]
(**4**)					
O3–H3	0.82	1.627	162.27	2.421	O2
O8–H8	0.82	1.588	175.48	2.407	O7

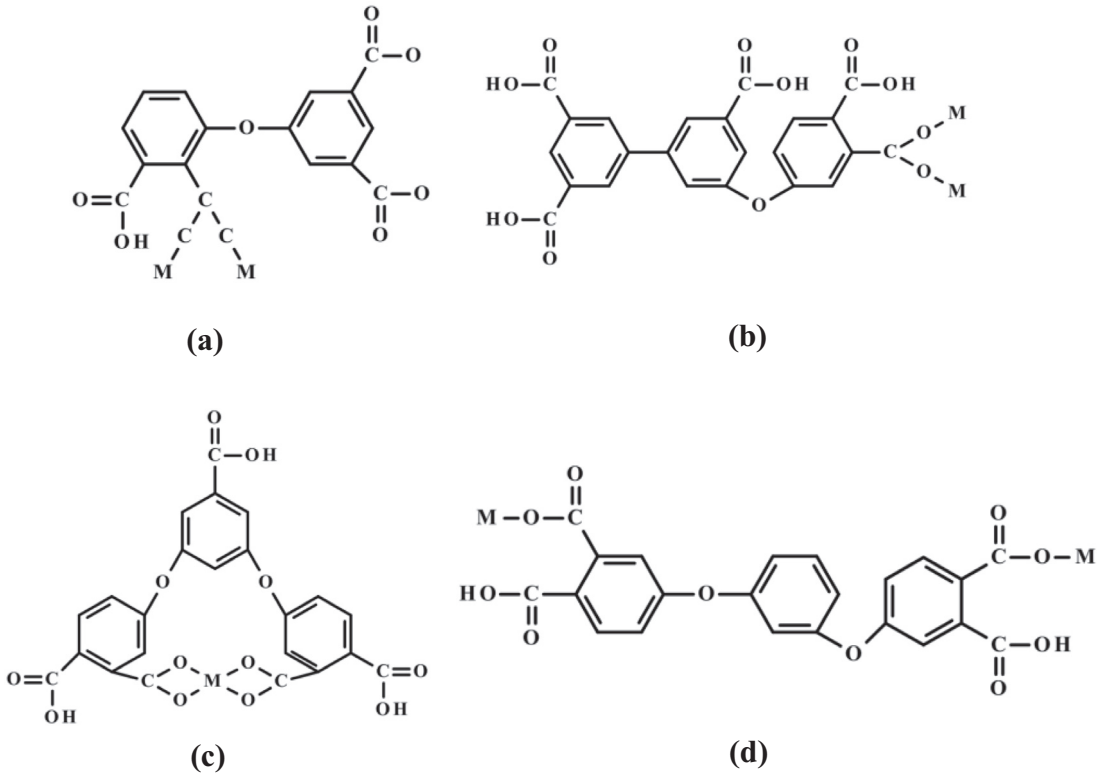

Scheme 2. The coordination modes of 2,2′,3,3′-H_4odpt (a), H_5dcpb (b and c) and H_2cpb (d) used in this study.

Table 4
Defined ring and relative parameters of the π–π interactions in **3**.

Cg(I) Cg(J)	Dist. centroids (Å	Dihedral angle (°)	Perp. dist. (IJ) (Å)	Perp. dist. (JI) (Å)
Cg(5) → Cg(4) #1	3.5564(19) Å	2.86(16)	3.3709(13)	3.3980(13)
Cg(9) → Cg(5) #1	3.6821(19)	3.3908(14)	3.3908(14)	3.3804(13)
Cg(9) → Cg(9) #1	3.8608(19)	3.4066(14)	0	3.4066(14)

Symmetry codes: #1 = 1 − *x*, 1 − *y*, −*z*
Cg(4): N(1) → C(24) → C(25) → C(26) → C(27) → C(28)→
Cg(5): N(2) → C(29) → C(30) → C(31) → C(32) → C(33)→
Cg(9): C(27) → C(28) → C(29) → C(30) → C(35) → C(34)→.

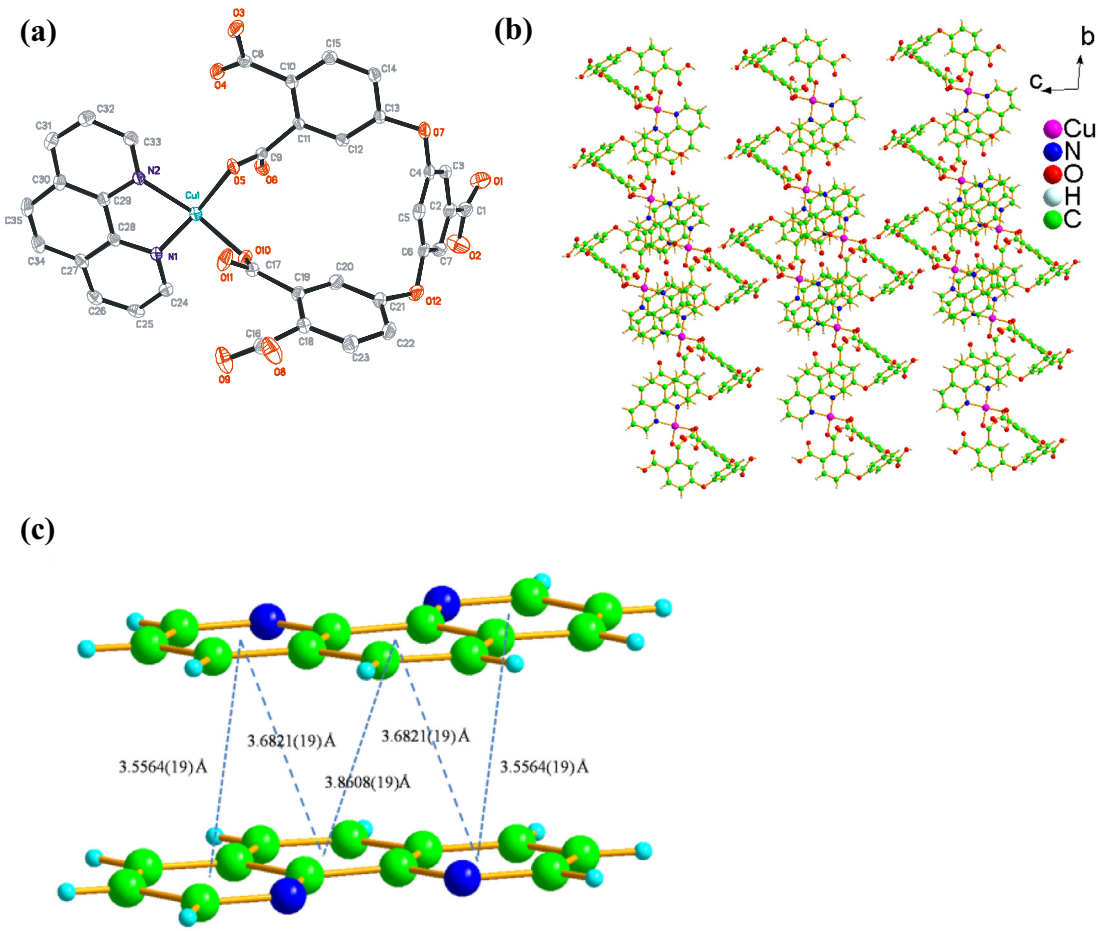

Fig. 2. (a) Asymmetric unit of [Cu(phen)(H_3dcpb)] (**3**). (b) Packing view of the 3D framework built with the aid of π–π stacking interactions along the *a*-axis for **3**. (c) Highlights of the π–π stacking interactions in **3**.

3.1.2. Compound **3**

In compound **3**, the copper(II) centre is four-coordinated by two nitrogen atoms from one phen ligand via a chelating mode, and two oxygen atoms from two different COO^- groups attached to the same H_5dcpb ligand. The Cu–O and Cu–N bond distances are comparable to the normal values [35], and the O(5)–Cu(1)–O(10), O(5)–Cu(1)–N(1), O(10)–Cu(1)–N(2) and N(1)–Cu(1)–N(2) bond angles are 91.81(8), 170.19(8), 166.56(8) and 83.07(9)°, respectively, implying that the Cu(II) atom displays a nearly square planar geometry. The partly deprotonated H_3dcpb^{2-} ligand acts as a bis-monodentate ligand to join one Cu(II) ion via the chelating mode, as depicted in Scheme 2. Although the two "O" atoms between two benzene rings in each H_3dcpb^{2-} ligand do not participate in the coordination to Cu(II) ions, they are important in the structure. With the presence of these "O" atoms, the H_3dcpb^{2-} ligands act as V-shaped, not linear ligands. It is the V-shaped configuration of the H_3dcpb^{2-} ligands that facilitates the H_3dcpb^{2-} ligands to display a variety of coordination modes. For example, the H_3dcpb^{2-} ligand in compound **2** displays a totally different coordination mode (bis-monodentate mode), as illustrated in Scheme 2(b). In compound **3**, the 0D [Cu(phen)(H_3dcpb)] units are packed into a 3D framework via π–π stacking interactions, with centroid–centroid distances ranging from 3.5564(19) to 3.8608(19) Å (Table 4) (Fig. 2).

3.1.3. Compound **4**

The crystal structure analysis reveals that compound **4** consists of 1D neutral [Mn(phen)$_2$(H_2cpb)] chains, as illustrated in Fig. 3(c). The Mn(II) ion, is six-coordinated by four nitrogen atoms from two different phen ligands and two oxygen atoms from two different

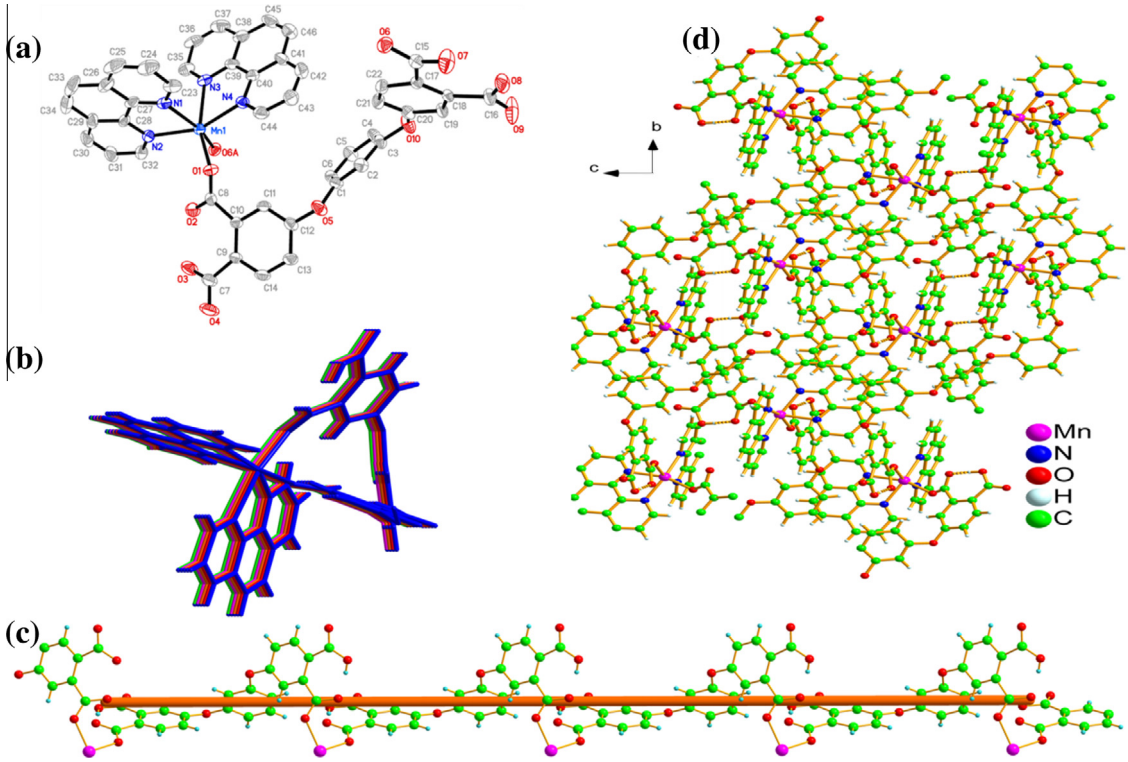

Fig. 3. (a) Asymmetric unit of [Mn(phen)$_2$(H$_2$cpb)] (**4**). (b) Packing view of the 1D [Mn(phen)$_2$(H$_2$cpb)] chain along the *b*-axis. (c). 1D helix chain of [Mn(phen)$_2$(H$_2$cpb)]. (d) 3D framework built with the aid of hydrogen-bonding interactions and π–π stacking interactions along the *a*-axis for **4**.

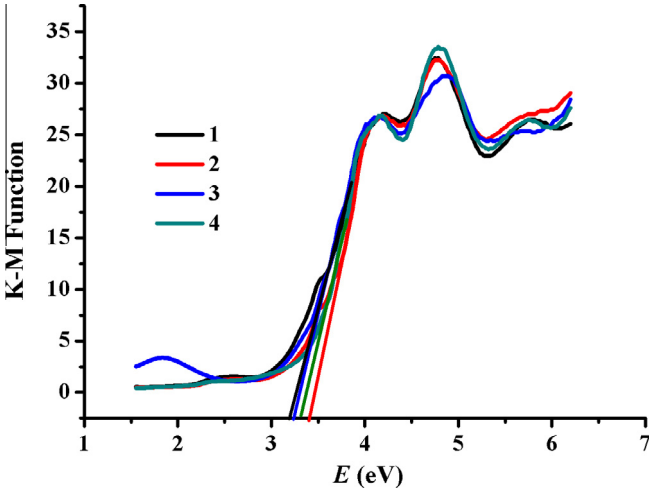

Fig. 4. Kubelka–Munk – transformed diffuse reflectance spectra of compounds **1**–**4**.

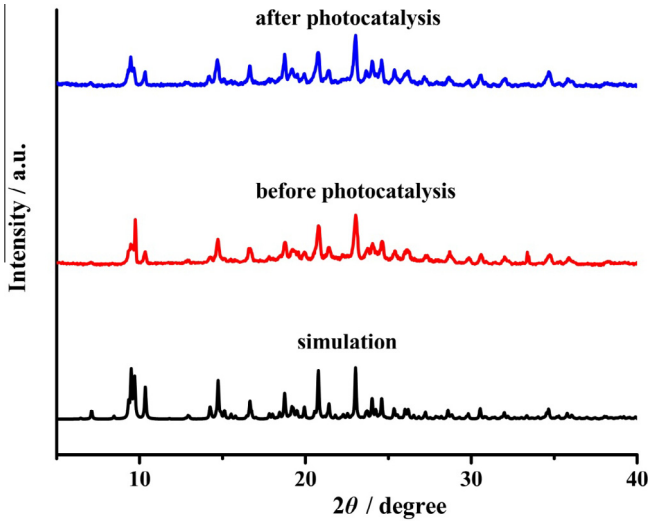

Fig. 5. PXRD patterns of compound **4** before and after the photocatalytic reaction and the simulated XRD pattern from the single crystal structure of compound **4**.

H$_2$cpb^{2-} ligands to complete a distorted octahedral geometry, in which one nitrogen and oxygen atom (O1 and N3) occupy the axial positions, and the remaining three nitrogen atoms (N1, N2 and N4) and one oxygen atom (O6$^{\#1}$) lie in the four sites of the equatorial plane, as shown in Fig. 3(a). The Mn–O and Mn–N bond distances are comparable with the normal values [36–38]. The partly deprotonated H$_2$cpb^{2-} ligands act as bis-monodentate bridging ligands to link two Mn(II) ions and form a 1D helix chain of [Mn(H$_2$cpb)], as shown in Fig. 3(c), and also play the role of a counter-ion to balance the charge of [Mn(phen)$_2$]$^{2+}$. Just as the H$_3$dcpb^{2-} ligands in compound **3**, the two "O" atoms between the two benzene rings

Table 5
Parameters of photodegradation reactions of MB dye and MO in compounds **1**–**4**.

	1		**2**		**3**		**4**		**4 + IPA**	
	k (min^{-1})	R^2	k (min^{-1})	R^2	k (min^{-1})	R^2	k (min^{-1})	R^2	k (min^{-1})	R^2
MB	0.0065	0.967	0.0117	0.992	0.0297	0.922	0.1131	0.933	0.019	0.925
MO	0.0033	0.991	0.006	0.997	0.0057	0.981	0.0365	0.997	0.0044	0.963

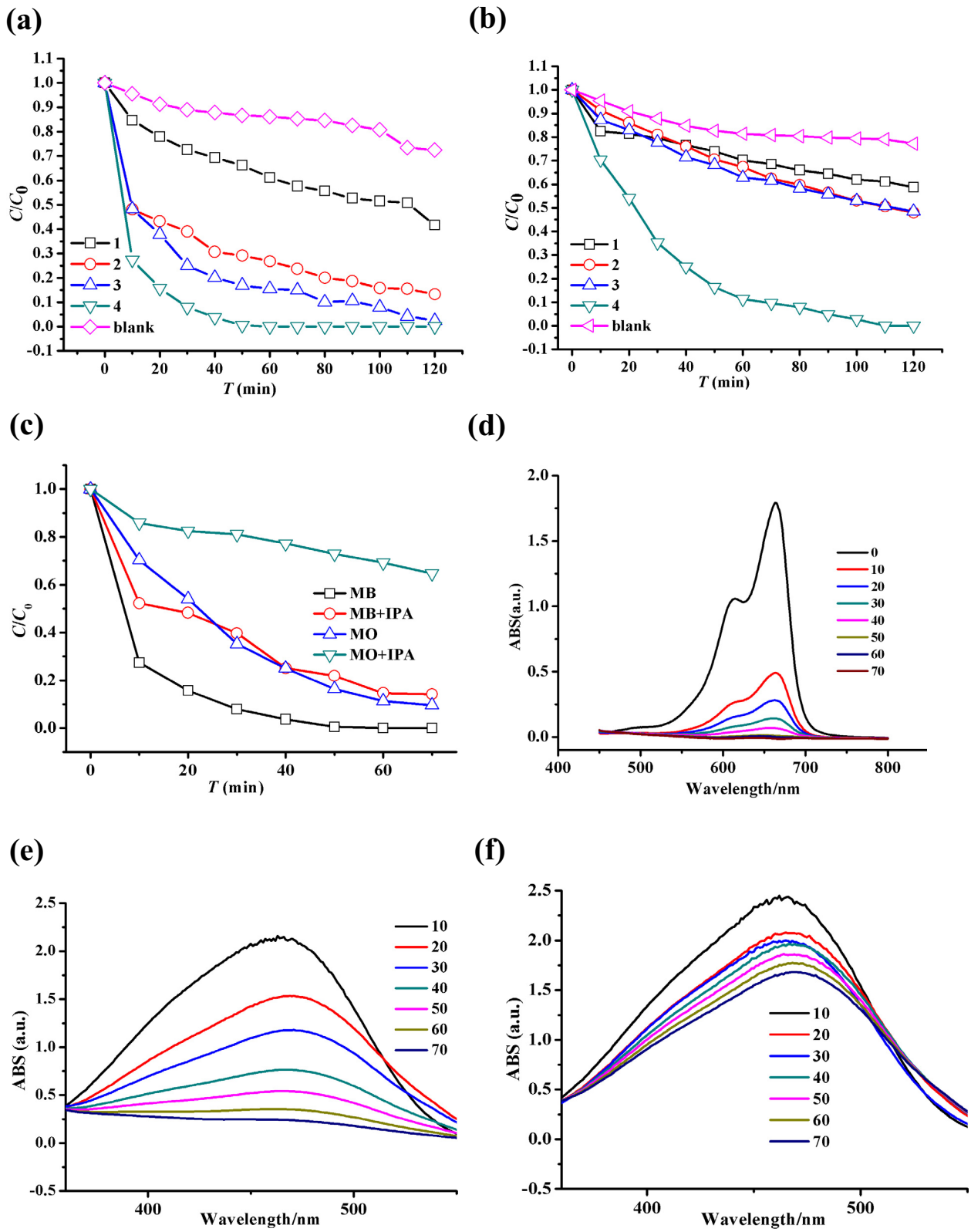

Fig. 6. (a) Plots of concentration vs. irradiation time for MB under irradiation by Hg lamp light with compounds **1**–**4** as photocatalysts. (b) Plots of concentration vs. irradiation time for MO under irradiation by Hg lamp light with compounds **1**–**4** as photocatalysts. (c) Plots of radical trapping with IPA in the system of photocatalytic degradation of MB and MO by compound **4** under UV light irradiation. (d) UV–Vis absorption spectra of an MB solution during the decomposition reaction under Hg lamplight irradiation in the presence of **4**. (e) UV–Vis absorption spectra of an MO solution during the decomposition reaction under Hg lamplight irradiation in the presence of **4**. (f) UV–Vis absorption spectra of an MO solution during the decomposition reaction under Hg lamplight irradiation in the presence of **4** and radical scavenger (IPA).

in each H_2cpb^{2-} ligand do not participate in coordination to the Mn(II) atoms, but they are important in the structure. With the presence of these "O" atoms, the H_2cpb^{2-} ligands act as flexible bis-monodentate ligands (Scheme 2(d)), which facilitates the construction of 1D helix chains of [Mn(H_2cpb)]. The adjacent 1D neutral [Mn(phen)$_2$(H_2cpb)] chains are packed into a 3D framework by hydrogen bonds, as listed in Table 4.

3.2. Optical energy gap

In order to explore the conductivity of the title compounds, measurement of the diffuse reflectivity for a powder sample was used to obtain its band gap E_g [39,40]. The band gap E_g was determined as the intersection point between the energy axis and the line extrapolated from the linear portion of the absorption edge in a plot of the Kubelka–Munk function F against energy E [41]. The Kubelka–Munk function, $F = (1 - R)^2/2R$, was converted from the recorded diffuse reflectance data, where R is the reflectance of an infinitely thick layer at a given wavelength [42]. The F versus E plots for compounds **1**–**4** are shown in Fig. 4, where steep absorption edges are displayed and the E_g values of all the compounds can be assessed as 3.2, 3.3, 3.2 and 3.4 eV, respectively, implying that **1**–**4** show selective absorption in the ultraviolet spectral region [43,44].

3.3. Photocatalytic activity

As we all know, coordination compounds have already been used for new photocatalytic materials in view of their potential applications in the degradation of organic pollutants [16]. The photocatalytic performances of compounds **1**–**4** for the photodegradation of MB and MO were carried out under UV irradiation. Additionally, control experiments on the photodegradation of MB and MO were performed. In order to confirm the powder purities of the title compounds used in this experiment, powder X-ray diffraction was conducted, and the results revealed that the powder X-ray patterns closely match the corresponding simulated patterns from their single X-ray crystal structure data. A comparison between the powder X-ray patterns and simulated patterns of compound **4** is illustrated in Fig. 5. The photocatalytic activities of **1**–**4** were monitored by measuring the maximum absorbance intensity at $\lambda = 463$ and 664 nm, characteristics of the targets MO and MB, respectively.

The efficiencies of the MB and MO's degradation in compounds **1**–**4** after the dark adsorption equilibrium was achieved are shown in Fig 5(a) and (b). All the data for the degradation efficiencies were the average values of three parallel tests. It can be seen that the photocatalytic activities of MB degradation increased from 27.5% (control experiment without any photocatalyst) to 58.4, 86.7, 97.6 and 99.9% with **1**, **2**, **3** and **4** as photocatalysts, respectively, under UV light irradiation for 120 min, and the MO degradation efficiency increased from 22.8% (without any photocatalyst) to 41.3, 52.1, 51.5 and 99.9% in the presence of **1**, **2**, **3** and **4**, respectively, under the same conditions up to 120 min. In fact, The MB degradation in the presence of **4** was nearly complete (99.7%) after 50 min. Additionally, all the photodegradation reactions of the MB and MO dyes with these four photocatalysts followed a pseudo-first-order kinetics model, as evidenced by the linear plot of ln(C/C_0) versus reaction time t. The pseudo-first-order rate constants (k) and the corresponding square of the correlation coefficients (R^2) for the photocatalytic degradation of MB and MO with **1**, **2**, **3** and **4** as photocatalysts are listed in Table 5.

As seen from Fig. 6(d) and (e), when the simulated wastewater samples containing MB and MO were irradiated under UV light, the maximum absorption peaks of MB and MO decreased obviously with reaction time in the presence of **4**. Furthermore, no other new peaks were observed during the process of degradation, see Fig. 6(d) and (e), indicating that photocatalyst **4** did not cause new pollutants to emerge.

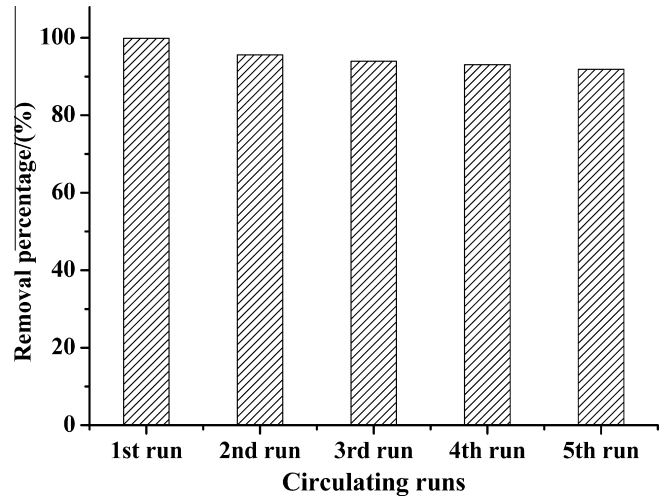

Fig. 7. The cycling runs of the degradation of MB (10 mg/L) over compound **4**/UV light system.

The recyclability of compound **4**, the most efficient photocatalyst in this study, was checked by circulating runs in the photocatalytic degradation of MB over the compound **4**/UV light system. The results in Fig. 7 show that the photocatalytic degradation performance of compound **4** remained almost unchanged after five runs for decompose MB, implying that photocatalyst **4** is very stable and can be used for the repeated decomposition of MB. Furthermore, the PXRD diffraction patterns and SEM images of the used photocatalyst were found be similar to those of the as-prepared photocatalyst before the reactions, as illustrated in Figs. 5 and 8, indicating that there is no noticeable change in the crystallographic structure and morphology of the photocatalyst after five reaction runs. These results demonstrate that compound **4** was stable under the experimental reaction conditions, and could be used circularly for several runs.

In the presence of UV light, there is an electron transfer from the highest occupied molecular orbital (HOMO) to the lowest unoccupied molecular orbital (LUMO) [16,45–47]. The HOMO is mainly contributed by O and/or N 2p bonding orbitals, and the LUMO is mainly contributed by empty M (like Mn) orbitals. The electron of the excited state in the LUMO is usually very easily lost, while the HOMO strongly demands one electron to return to its stable state [16,17]. Therefore, one electron is captured from water molecules, which are oxygenated into the ·OH active species [16,47–49]. The ·OH radicals could then decompose MB or MO efficiently to complete the photocatalytic process [47–49].

It should be pointed out that some coordination compounds are labelled as semiconductors based on their optical transition properties and electrochemical and photochemical activities [16,17,45]. However, recently Gascon and coworkers pointed out that such semiconducting behavior only occurs in a very limited subset of coordination compounds [45]. As to photocatalysis, coordination compounds should be treated as molecular catalysts rather than as typical semiconductors. To understand the photocatalysis mechanisms of coordination compounds, they suggested that the terminology of the HOMO–LUMO gap should be utilized to describe the discrete character of the light-induced transitions [45]. Therefore, it is easy to understand that only compound **4** exhibits good photocatalytic performance on both the MB and MO degradation, although all compounds **1**–**4** have nearly identical optical energy gaps (E_g = 3.2, 3.3, 3.2 and 3.4 eV for **1**, **2**, **3** and **4**, respectively)[17].

A possible mechanism can be proposed to clarify the degradation of the organic dyes in the presence of **4** as a photocatalyst

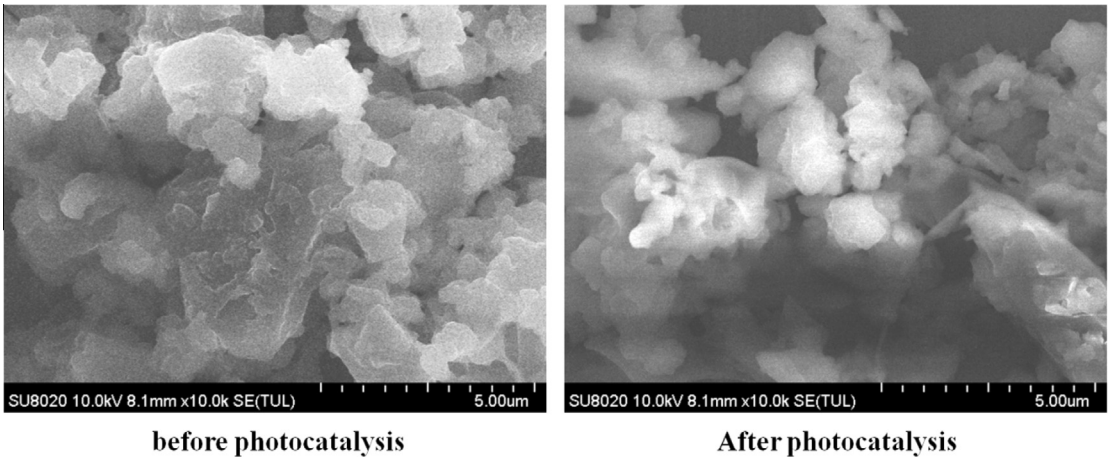

Fig. 8. SEM micrographs of compound **4** before and after the photocatalytic reaction.

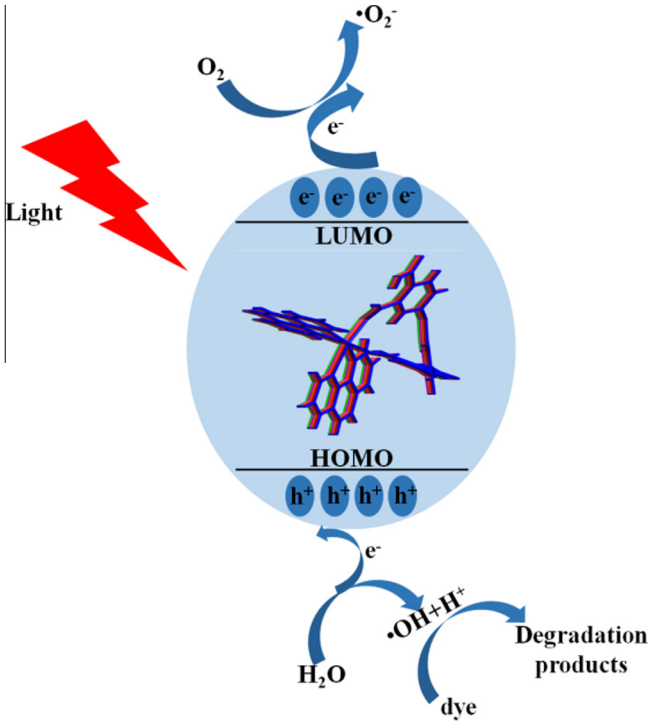

Scheme 3. A simplified model of the photocatalytic reaction mechanism of MB and MO with compounds **1**–**4**.

[17], as illustrated in Scheme 3. In order to confirm the proposed mechanism, radicals trapping experiments were applied to detect the main oxidative species in the photocatalytic process [50]. The results affirmed that the addition 1 mM of isopropanol (IPA) as a radical scavenger inhibited greatly the degradation efficiencies of MO (giving a decrease from 90.4(2)% without IPA to 35.3(2)% with IPA as a scavenger) and MB (giving a decrease from 99.7(2)% to 85.8(1)%) under UV light irradiation after 70 min, which suggest that oxygenous radicals are the main active species in this system, as illustrated in Fig. 6(c), (e) and (f).

4. Conclusions

In summary, the synthesis of four novel metal–organic frameworks has been accomplished by employing the hydrothermal method. Compounds **1**–**4** have been characterized using a variety of techniques, namely X-ray single crystal diffraction analysis, FTIR, UV–Vis diffuse spectroscopy and CHN element analysis. The crystal structure analysis revealed that compounds **1**–**3** consist of discrete neutral [M(phen)(L)] units, forming 3D frameworks via hydrogen bonding interactions or π–π stacking interactions, while compound **4** is built up from 1D helix chains, forming a 3D framework via hydrogen bonding interactions. All compounds **1**–**4** have nearly identical optical energy gaps (E_g = 3.2, 3.3, 3.2 and 3.4 eV for **1**, **2**, **3** and **4**, respectively), but show different photocatalytic degradation of MB and MO under UV light irradiation, implying the HOMO–LUMO gap is suitable to describe the photocatalytic performances. Additionally, a possible photocatalytic mechanism was proposed and discussed, which was confirmed by trapping experiments of radicals with the addition of isopropanol as a radical scavenger. This work opens a new prospective and a feasible strategy for the application of coordination compounds in photocatalytic degradation of organic dye pollutants. Further research should be carried out to clarify the photocatalytic activities on other organic pollutants.

Acknowledgements

We give thanks for the financial support from the Beijing Natural Science Foundation, China & Scientific Research Key Program of Beijing Municipal Commission of Education (KZ201410016018), the Training Program Foundation for the Beijing Municipal Excellent Talents (2013D005017000004), the Importation and Development of High-Caliber Talents Project of Beijing Municipal Institutions (CIT&CD201404076), the Scientific Research Common Program of Beijing Municipal Commission of Education (KM201510016017), China and the Open Research Fund Program of Key Laboratory of Urban Stormwater System and Water Environment (Ministry of Education).

Appendix A.

CCDC 1033347–1033350 contain the supplementary crystallographic data for this paper. These data can be obtained free of charge from The Cambridge Crystallographic Data Centre via www.ccdc.cam.ac.uk/data_request/cif, or from the Cambridge Crystallographic Data Centre, 12 Union Road, Cambridge CB2 1EZ, UK; fax: +44 1223 336 033; or e-mail: deposit@ccdc.cam.ac.uk.

References

[1] C.-C. Wang, H.-Y. Li, G.-L. Guo, P. Wang, Transition Met. Chem. 38 (2013) 275.
[2] C.-C. Wang, G.-L. Guo, P. Wang, Transition Met. Chem. 38 (2013) 455.

[3] C.-C. Wang, G. Guo, P. Wang, J. Mol. Struct. 1032 (2013) 93.
[4] C.-C. Wang, P. Wang, G.-S. Guo, Transition Met. Chem. 35 (2010) 721.
[5] C.-C. Wang, Z. Wang, F. Gu, G. Guo, J. Mol. Struct. 979 (2010) 92.
[6] S.A. Sapchenko, D.G. Samsonenko, V.P. Fedin, Polyhedron 55 (2013) 179.
[7] S.S. Pedro, P. Brandão, F.N. Shi, J.C.G. Tedesco, M.S. Reis, Polyhedron 81 (2014) 210.
[8] S. Ma, H.-C. Zhou, Chem. Commun. 46 (2010) 44.
[9] R.E. Morris, P.S. Wheatley, Angew. Chem., Int. Ed. 47 (2008) 4966.
[10] M.P. Suh, H.J. Park, T.K. Prasad, D.-W. Lim, Chem. Rev. 112 (2011) 782.
[11] J.-R. Li, R.J. Kuppler, H.-C. Zhou, Chem. Soc. Rev. 38 (2009) 1477.
[12] J.-R. Li, Y. Ma, M.C. McCarthy, J. Sculley, J. Yu, H.-K. Jeong, P.B. Balbuena, H.-C. Zhou, Coord. Chem. Rev. 255 (2011) 1791.
[13] K. Sumida, D.L. Rogow, J.A. Mason, T.M. McDonald, E.D. Bloch, Z.R. Herm, T.-H. Bae, J.R. Long, Chem. Rev. 112 (2011) 724.
[14] J. Lee, O.K. Farha, J. Roberts, K.A. Scheidt, S.T. Nguyen, J.T. Hupp, Chem. Soc. Rev. 38 (2009) 1450.
[15] H.-P. Jing, C.-C. Wang, Y.-W. Zhang, P. Wang, R. Li, RSC Adv. 4 (2014) 54454–54462. *edit*.
[16] C.-C. Wang, J.-R. Li, X.-L. Lv, Y. Zhang, G. Guo, Energy Environ. Sci. 7 (2014) 2831.
[17] C.-C. Wang, H.-P. Jing, P. Wang, S.-J. Gao, J. Mol. Struct. 1080 (2015) 44.
[18] C.-C. Wang, H.-P. Jing, P. Wang, J. Mol. Struct. 1074 (2014) 92.
[19] P. Du, Y. Yang, Y.-Y. Liu, Y.-C. He, H.-M. Zhang, J.-F. Ma, Polyhedron 70 (2014) 180.
[20] L. Zhang, L. Liu, M. Li, C. Huang, H. Xu, H.-W. Hou, Y.-T. Fan, Polyhedron 83 (2014) 197.
[21] Q.-L. Lu, J. Luan, X.-L. Wang, H.-Y. Lin, M. Le, G.-C. Liu, Polyhedron 83 (2014) 108.
[22] C. Wang, Z. Xie, K.E. deKrafft, W. Lin, J. Am. Chem. Soc. 133 (2011) 13445.
[23] C.-C. Wang, Y.-Q. Zhang, J. Li, P. Wang, J. Mol. Struct. 1083 (2014) 127.
[24] Y. Fu, D. Sun, Y. Chen, R. Huang, Z. Ding, X. Fu, Z. Li, Angew. Chem. 124 (2012) 3420.
[25] L. Shen, S. Liang, W. Wu, R. Liang, L. Wu, Dalton Trans. 42 (2013) 13649.
[26] R. Liang, L. Shen, F. Jing, W. Wu, N. Qin, R. Lin, L. Wu, Appl. Catal. B: Environ. 162 (2015) 245.
[27] C.-C. Wang, P. Wang, L.L. Feng, Transition Met. Chem. 37 (2012) 225.
[28] S. Zang, Y. Su, Y. Li, Z. Ni, Q. Meng, Inorg. Chem. 45 (2005) 174.
[29] J.-Q. Liu, J. Wu, T. Wu, Synth. React. Inorg., Met.-Org., Nano-Met. Chem. 40 (2010) 231.
[30] Bruker AXS, SMART, Version 5.611, Bruker AXS, Madison, WI, USA, 2000.
[31] Bruker AXS, SAINT, Version 6.28, Bruker AXS, Madison, WI, USA, 2003.
[32] SADABS, V2.03, Bruker AXS, Madison, WI, 2000.
[33] G.M. Sheldrick, SHELX-97, Göttingen University, Germany, 1997.
[34] L. Schlechte, V. Bon, R. Grünker, N. Klein, I. Senkovska, S. Kaskel, Polyhedron 44 (2012) 179.
[35] S. Gulli, J.C. Daran, R. Poli, Eur. J. Inorg. Chem. 2011 (2011) 1666.
[36] Y. Qi, Y. Wang, Polyhedron 73 (2014) 133.
[37] M. Bagherzadeh, F. Ashouri, M. Đaković, Polyhedron 69 (2014) 167.
[38] H. Günay, A.T. Çolak, O.Z. Yeşilel, S. Keskin, O. Büyükgüngör, Polyhedron 48 (2012) 199.
[39] W.-J. Ji, Q.-G. Zhai, S.-N. Li, Y.-C. Jiang, M.-C. Hu, Inorg. Chem. Commun. 24 (2012) 209.
[40] P. Du, Y. Yang, J. Yang, B.-K. Liu, J.-F. Ma, Dalton Trans. 42 (2013) 1567.
[41] J.I. Pankove, Optical Processes in Semiconductors, Courier Dover Publications, 2012.
[42] W.W. Wendlandt, H.G. Hecht, Reflectance Spectroscopy, Interscience, New York, 1966.
[43] K.C. Stylianou, R. Heck, S.Y. Chong, J. Bacsa, J.T. Jones, Y.Z. Khimyak, D. Bradshaw, M.J. Rosseinsky, J. Am. Chem. Soc. 132 (2010) 4119.
[44] K.G. Laurier, F. Vermoortele, R. Ameloot, D.E. De Vos, J. Hofkens, M.B. Roeffaers, J. Am. Chem. Soc. 135 (2013) 14488.
[45] M.A. Nasalevich, M. van der Veen, F. Kapteijn, J. Gascon, CrystEngComm 16 (2014) 4919.
[46] H.A. Lopez, A. Dhakshinamoorthy, B. Ferrer, P. Atienzar, M. Alvaro, H. Garcia, J. Phys. Chem. C 115 (2011) 22200.
[47] P. Mahata, G. Madras, S. Natarajan, J. Phys. Chem. B 110 (2006) 13759.
[48] Z.-T. Yu, Z.-L. Liao, Y.-S. Jiang, G.-H. Li, J.-S. Chen, Chem. Eur. J. 11 (2005) 2642.
[49] X.-L. Wang, J. Luan, F.-F. Sui, H.-Y. Lin, G.-C. Liu, C. Xu, Cryst. Growth Des. 13 (2013) 3561.
[50] H. Zhang, R. Zong, J. Zhao, Y. Zhu, Environ. Sci. Technol. 42 (2008) 3803.